

Counting the Eigenvalues of the Laplace Operator on Some Convex Domains

Aidan Tillman* and Yuzhi Liu†

Project Advisor: Stuart Brorson‡

Abstract

We define algorithms for computing the eigenvalue counting functions (ECFs) of the Laplacian with Dirichlet and Neumann boundary conditions for a variety of convex 2D and 3D domains using floating point precision in Python. These domains include the square, disk, ball, cube, and cylinder. We use these computed ECFs to validate Polya’s conjecture on these domains. The conjecture has not been proven in completeness on the ball, so this work presents numerical evidence to the positive. We also use these calculations to study the potential geometric information in the lower-order terms of the asymptotics by comparing ECFs between different shapes. We do this by subtracting the like terms in the asymptotics of the ECFs to draw out the lower-order information. In the 3D case, a difference can be seen in the lower-order asymptotics of a cube and cylinder with the same volume and surface area. In particular, the cube’s $o(k^2)$ term has a larger variance than the cylinder’s term, and in both cases, the term is mostly positive.

Contents

| | | |
|----------|------------------------------|-----------|
| 1 | Introduction | 2 |
| 2 | 2D Geometries | 3 |
| 2.1 | The Square of Sidelength s | 4 |
| 2.2 | The Unit Disk | 6 |
| 2.3 | Comparison of 2D Geometries | 9 |
| 3 | 3D Geometries | 10 |
| 3.1 | The Unit Ball | 10 |
| 3.2 | The Unit Cube | 13 |
| 3.3 | The Cylinder | 14 |
| 3.4 | Comparison of 3D Geometries | 15 |
| 4 | Future Work | 17 |
| A | List of Symbols | 19 |

*Department of Bioengineering, Northeastern University, Boston, Massachusetts, USA,
tillman.ai@northeastern.edu

†Department of Mathematics, University of Michigan Ann Arbor, Ann Arbor, Michigan, USA,
liu.yuzhi@northeastern.edu

‡Department of Mathematics, Northeastern University, Boston, Massachusetts, USA,
s.brorson@northeastern.edu

1 Introduction

In this paper, we consider the mathematical properties of the Laplacian differential operator, defined in d -dimensional Cartesian coordinates as

$$\nabla^2 = \sum_{i=1}^d \frac{\partial^2}{\partial x_i^2}. \quad (1)$$

In particular, we are interested in the distribution of the eigenvalue spectrum of the Laplacian in different geometries. Similar to eigenvalue problems in finite-dimensional linear algebra, the eigenvalues of the Laplacian on a bounded domain $\Omega \subset \mathbb{R}^d$ are defined with the following partial differential equation (PDE):

$$\nabla^2 u = -\lambda u. \quad (2)$$

Equation (2) is called the *Helmholtz* equation. For the duration of the paper, we consider only the following two types of boundary conditions:

Definition 1.1 Let $\Omega \subset \mathbb{R}^d$ be bounded and have a Lipschitz continuous boundary $\partial\Omega$. Let \hat{n} be a normal vector field on $\partial\Omega$. Then, given a PDE of unknown u , such as (2), let the *Dirichlet* boundary conditions (BCs) on Ω be $u(x) = 0, \forall x \in \partial\Omega$. Let the *Neumann* BCs be $\frac{\partial u}{\partial \hat{n}} = \nabla(u(x)) \cdot \hat{n}(x) = 0, \forall x \in \partial\Omega$.

Dirichlet conditions fix u at the boundary and Neumann conditions fix the flux of u across the boundary. Thus, the Neumann conditions given in definition 1.1 are also called No Flux BCs. Non-trivial ($u \neq 0$) solution pairs (λ, u) are respectively called *eigenvalues* and *eigenfunctions* of the Laplacian on Ω . By solving the eigenvalue problem (2) with these different boundary conditions, we produce two distinct spectra of the Laplacian on Ω : the Dirichlet spectrum and the Neumann spectrum. It is known from linear elliptic PDE theory (see chapter 6 in [6]) that these spectra are discrete, any given eigenvalue is real, non-negative, and of finite multiplicity, and that the eigenvalues accumulate up to $+\infty$. Specifically, the Dirichlet and Neumann eigenvalues on Ω can be sorted into monotonically increasing sequences (λ_n) and (μ_n) respectively such that

$$\begin{aligned} 0 < \lambda_1 \leq \lambda_2 \leq \dots \leq \lambda_n \leq \dots \\ 0 = \mu_1 \leq \mu_2 \leq \dots \leq \mu_n \leq \dots \end{aligned} \quad (3)$$

We can thus define a counting function for these spectra as follows:

Definition 1.2 Let (λ_n) and (μ_n) be the sequences of ordered Dirichlet and Neumann eigenvalues for a bounded set $\Omega \subset \mathbb{R}^n$. The Dirichlet and Neumann eigenvalue counting functions (ECF) for the Laplacian on Ω , $\mathcal{N}_\Omega^D(k)$ and $\mathcal{N}_\Omega^N(k)$ are described as

$$\begin{aligned} \mathcal{N}_\Omega^D(k) &= \#\{n : \lambda_n \leq k^2\}, \\ \mathcal{N}_\Omega^N(k) &= \#\{n : \mu_n \leq k^2\}. \end{aligned} \quad (4)$$

Observe that in (4) we count the number of eigenvalues less than the square of the input, rather than just the input. This normalization is helpful for computation and a standard notation used in literature [7].

Our study focuses on the asymptotic behavior of the ECFs on different geometries. To begin, we define *Weyl's law* for the Laplacian eigenvalue counting functions:

Theorem 1.3 Let $\mathcal{N}_\Omega(k)$ be either the Neumann or Dirichlet counting function for the bounded set $\Omega \subset \mathbb{R}^d$. Then it has the following one term asymptotics:

$$\mathcal{N}_\Omega(k) = C_d |\Omega|_d k^d + o(k^d), \quad (5)$$

where

$$C_d = \frac{1}{(4\pi)^{\frac{d}{2}} \Gamma(\frac{d}{2} + 1)},$$

with $\Gamma(x)$ as the Gamma function, and $|\Omega|_d$ is the d -dimensional volume of Ω .

Proof Originally proven by Weyl in [18].

Weyl's law is the basis on which most study on the asymptotic distribution of Laplacian eigenvalues is based, with much study on improving this approximation. Weyl conjectured a further improvement in the following two-term law for sets with piecewise-smooth boundaries [19]:

$$\mathcal{N}_\Omega(k) = C_d |\Omega|_d k^d \pm C_{b,d} |\partial\Omega|_{d-1} k^{d-1} + o(k^{d-1}), \quad (6)$$

where

$$C_{b,d} = \frac{C_{d-1}}{4},$$

and the sign is a plus for Neumann boundary conditions and a minus for Dirichlet boundary conditions. This two-term statement remains unsolved in generality, but it has been proven for convex analytic domains [15]. These asymptotic terms define a distinct relationship between the geometry of shapes and the behavior of the Laplacian operator on their domains. Observe that, for sufficiently large k , (6) implies the following set of inequalities:

$$\mathcal{N}_\Omega^D(k) \leq C_d |\Omega|_d k^d \leq \mathcal{N}_\Omega^N(k). \quad (7)$$

George Polya made the stronger conjecture that these inequalities are true not just for large k , but for any $k \geq 0$. It is this conjecture that we focus our study on. The left inequality is referred to as the Dirichlet conjecture and the right inequality is referred to as the Neumann conjecture. Polya proved the Dirichlet conjecture for *tiling* sets of \mathbb{R}^d , and R. Kellner later proved the Neumann conjecture for these sets [10]. Recently, Filonov et al proved the complete conjecture for the unit disk and the Dirichlet conjecture for the d -dimensional unit ball [7]. Furthermore, for sets on which the conjecture is proven, the conjecture is also proven on their Cartesian products:

Proposition 1.4 Let $\Omega_1 \subset \mathbb{R}^{d_1}$ with $d_1 \geq 2$ be a set on which Polya's conjecture is true and let $\Omega_2 \subset \mathbb{R}^{d_2}$ be bounded. Then the Cartesian product $\Omega_1 \times \Omega_2 \subset \mathbb{R}^{d_1+d_2}$ also satisfies Polya's conjecture.

Proof The Dirichlet case is Theorem 2.8 in [12] and the Neumann case is Corollary 1.4 in [8].

It is a goal of this paper to numerically check Polya's conjecture for a variety of 2D and 3D convex geometries using algorithms with floating point accuracy. These include sets where the conjecture has been proven, but they also include the unit ball, where the complete conjecture is unproven, so our work represents new results in those cases. Furthermore, it is known in general that non-congruent shapes can possess the same eigenvalue spectra [5], so we were also interested in comparing shapes with the same volume, surface area, etc. per Weyl's two-term law. Differences in counting function behavior for different shapes with the same asymptotic Weyl terms could imply that geometric information about these differences is encoded in the remaining $o(k^{d-1})$ term in the asymptotics. Therefore, comparing these counting functions highlights potential differences. We accomplish this task by normalizing the computed ECFs via subtracting the leading Weyl terms to ensure the observed behavior comes from the lower-order terms. In this process, we also provide new visualizations of the ECFs for these geometries. Specific Python scripts can be found in the supplementary material.

2 2D Geometries

We now consider two geometries in \mathbb{R}^2 . We start with the square and move to the disk. Polya's conjecture has been proven for both shapes, so our computations serve as visualizations of the inequalities

for these shapes. Furthermore, since the leading term $C_2|\Omega|_2k^2$ is solely a function of a shape's area, we restrict our geometric parameters such that the shapes all have the same area, π . The leading asymptotic term for this area is

$$\mathcal{N}_\Omega(k) = \frac{k^2}{4} + o(k). \quad (8)$$

Comparing the ECFs of 2D shapes with equal areas highlights how more geometric information than just the area of shape is captured in these counting functions. This concept will be more heavily explored in section 3.

2.1 The Square of Sidelength s

Firstly, we examine the case of the square of sidelength s whose bottom left corner is the origin. The Helmholtz equations in Cartesian coordinates (x, y) is simply expressed as

$$\frac{\partial^2 u}{\partial x^2} + \frac{\partial^2 u}{\partial y^2} = -\lambda u. \quad (9)$$

The Dirichlet BCs on $u(x, y)$ are $u(x, s) = u(x, 0) = u(0, y) = u(s, y) = 0$ and the Neumann BCs are $\frac{\partial u}{\partial x}|_{y=0} = \frac{\partial u}{\partial x}|_{y=s} = \frac{\partial u}{\partial y}|_{x=0} = \frac{\partial u}{\partial y}|_{x=s} = 0$. Using the separation of variables, it can be seen that, with $n, m \in \mathbb{N}$, the Dirichlet eigenfunctions on the square are

$$u_{nm}(x, y) = \sin\left(\frac{n\pi x}{s}\right) \cdot \sin\left(\frac{m\pi y}{s}\right). \quad (10)$$

Now, expanding to $n, m \in \mathbb{N} \cup \{0\}$, the Neumann eigenfunctions on the square are

$$u_{nm}(x, y) = \cos\left(\frac{n\pi x}{s}\right) \cdot \cos\left(\frac{m\pi y}{s}\right). \quad (11)$$

From (10) and (11) it can be seen that the eigenvalues in both cases are of the form

$$\lambda_{nm} = \frac{\pi^2}{s^2}(n^2 + m^2), \quad (12)$$

with the only difference being whether one allows n and m to be zero. Observe per (12) that it is often possible to find multiple pairs (n_1, m_1) and (n_2, m_2) such that $\lambda_{n_1 m_1} = \lambda_{n_2 m_2}$. When $n_1 \neq m_1$, the trivial case is found by simply transposing the indices such that $n_1 = m_2$ and $m_1 = n_2$. Here the two pairs produce the same eigenvalue but distinct eigenfunctions, so they impact the eigenvalue's multiplicity. In general, the multiplicity of an arbitrary eigenvalue of the square is a number theory problem. The following known proposition gives some light to the multiplicity of a given Dirichlet eigenvalue:

Proposition 2.1.1[11] Let λ be a number of the form $\lambda = m^2 + n^2$ for $n, m \in \mathbb{N}$. If λ has a prime factorization of the form $\lambda = 2^\alpha p_1^{r_1} \dots p_k^{r_k} q_1^{s_1} \dots q_l^{s_l}$, where the p_i are of the form $4t + 1$ and the q_i are of the form $4t + 3$, then the multiplicity of λ is

$$\prod_{i=1}^k (r_i + 1). \quad (13)$$

As long as the pre-factor of $\frac{\pi^2}{s^2}$ is considered, the identity (13) can be used to find the multiplicity of any given Dirichlet eigenvalue. However, it is not useful for handling Neumann eigenvalues, and it does not give a method for generating eigenvalues, so it is not useful for computing the ECFs of a square. However, it can be useful for creating regression tests to ensure any square ECF algorithm is producing the correct multiplicity for a given eigenvalue.

To calculate the square ECFs, we used a naive, greedy algorithm that used a double for-loop to check every possible set of (n, m) within a finite range to see if they produce a valid eigenvalue, as described in algorithm 1. This ensured that we captured every possible eigenvalue below k^2 .

Algorithm 1 Calculating the Dirichlet ECF on a square with sidelength s

Input Maximum value k

Step 1: init $nMax = \lfloor k \rfloor$

Step 2: init eigenvalues as empty list

Step 3:

For $n = 1, \dots, nMax$

· **For** $m = 1, \dots, nMax$

· Find candidate λ_{nm} using eqn (12)

· **If** candidate $\lambda_{nm} > k^2$, break

· **Elseif** candidate not in eigenvalues, add to eigenvalues with multiplicity 1

· **Elseif** candidate is in eigenvalues, multiplicity $+= 1$

Step 3: **Sort** eigenvalues in ascending order

Step 4: Iterate through the ordered list starting from the second element, and for each element add the multiplicity value of the previous element to that of the current element

Output Set of tuples of the eigenvalues and the number of eigenvalues less than or equal to that eigenvalue.

Per the goal of comparing the ECFs of shapes whose asymptotic term is defined by (8), we applied algorithm 1 to compute the ECFs of the square with sidelength $s = \sqrt{\pi}$. The results of this computation are documented in figure 1.

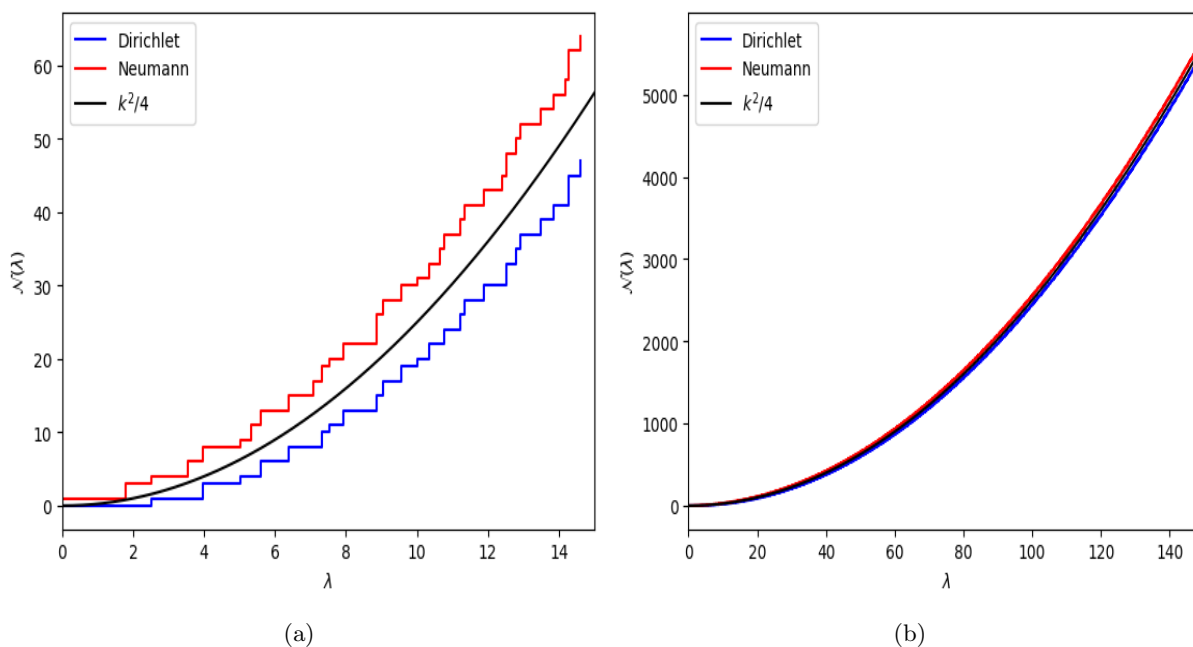


Figure 1: The Calculated ECFs and the leading Weyl Term on the Square with sidelength $\sqrt{\pi}$ up until (a) $k = 15$ and (b) $k = 150$

2.2 The Unit Disk

Our next 2D object of consideration is the disk of unit radius centered at the origin. Filonov et al recently analytically proved the conjecture (7) for the disk [7]. In fact, the unit disk is the only non-tiling subset of \mathbb{R}^2 for which the conjecture has been proven. Thus, here we visualize this theorem by calculating the ECFs on the disk. Here we use the standard Polar coordinate transformation $(x, y) \rightarrow (r, \phi)$, where r is the distance from the origin and ϕ is the angle from the x-axis. The Helmholtz equation in Polar coordinates is

$$\frac{\partial^2 u}{\partial r^2} + \frac{1}{r} \frac{\partial u}{\partial r} + \frac{1}{r^2} \frac{\partial^2 u}{\partial \phi^2} = -\lambda u. \quad (14)$$

The Dirichlet BCs are $u(1, \phi) = 0$ and the Neumann BCs are $\frac{\partial u}{\partial r}|_{r=1} = 0$. It is also necessary to take periodic BCs on ϕ such that $u(r, 0) = u(r, 2\pi)$. With these BCs, separation of variables can be applied such that, for $n \in \mathbb{N} \cup \{0\}$ and $m \in \mathbb{N}$, the Dirichlet eigenfunctions on the unit disk are

$$u_{nm}(r, \phi) = J_n(j_{n,m}r) \cdot (\sin(n\phi) + \cos(n\phi)), \quad (15)$$

and the Neumann eigenfunctions are

$$u_{nm}(r, \phi) = J_n(j'_{n,m}r) \cdot (\sin(n\phi) + \cos(n\phi)), \quad (16)$$

where $J_n(x)$ is the n th order Bessel function of the first kind, $j_{n,m}$ is the m th non-zero root of $J_n(x)$, $j'_{n,m}$ is the m th non-zero root of $\frac{dJ_n}{dx}$.

It is now necessary to describe Bessel functions and their properties.

Definition 2.2.1 Bessel functions of order n are solutions to Bessel's differential equation:

$$x^2 \frac{d^2 y}{dx^2} + x \frac{dy}{dx} + (x^2 - n^2)y = 0. \quad (17)$$

As a second-order differential equation, (17) has two independent solutions, denoted J_n and Y_n . However, Y_n diverges at zero and therefore is not continuous on $[0, 1]$ and can't be used to construct valid solutions to (14).

Remark: Equation (17) allows valid solution for any real number n , but the only valid solutions to (14) require n to be a nonnegative integer.

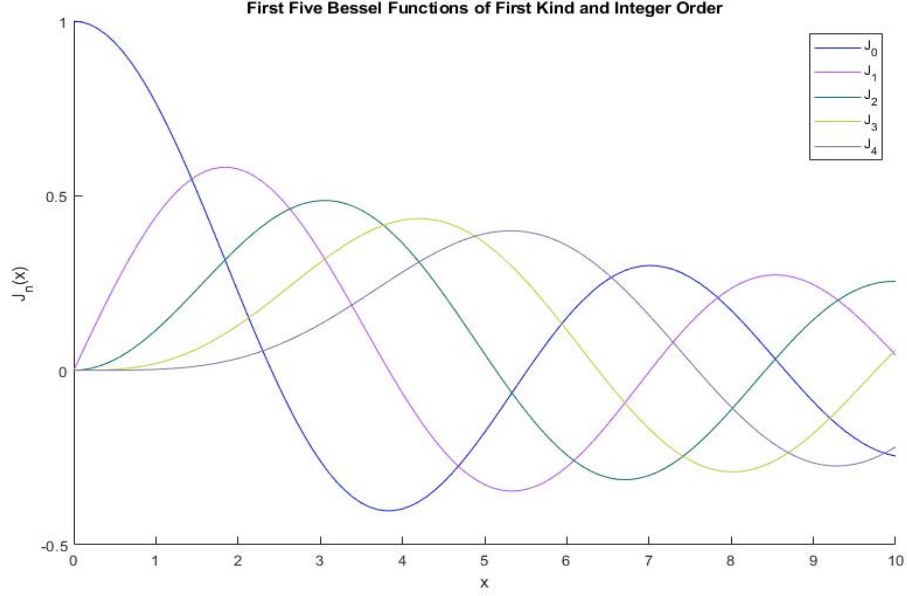


Figure 2: The First Five First-kind Bessel Functions of integer order, produced in Matlab

Figure 2 visualizes some relevant traits of the Bessel functions. Observe that they are oscillatory, as their asymptotics resemble a combination of sines and cosines. This also implies that the roots always "cross" the x-axis. For further detail, see [16]. Furthermore, the distribution of their roots has multiple established characteristics. Every J_n with $n > 0$ has a trivial root at zero. Firstly, the roots are interlaced based on order, as described by the following set of inequalities [13]:

$$j_{n,m} \leq j_{n+1,m} \leq j_{n,m+1}. \quad (18)$$

Next, the values of $j_{n,1}$ and $j'_{n,1}$, the first roots, grow as a function of n , which is encoded as:

$$n \leq j'_{n,1} < j_{n,1}. \quad (19)$$

For more details, see reference [13].

In the greater context of spectral geometry, the roots of Bessel functions play another important role as optimizers for the first non-zero eigenvalues of arbitrary geometries. Specifically, for a bounded $\Omega \subset \mathbb{R}^d$,

$$\mu_2(\Omega) \leq \left(\frac{|\mathbb{B}_d|}{|\Omega|} \right)^{\frac{2}{d}} (j'_{\frac{d}{2},1})^2 \leq \left(\frac{|\mathbb{B}_d|}{|\Omega|} \right)^{\frac{2}{d}} (j_{\frac{d}{2}-1,1})^2 \leq \lambda_1(\Omega). \quad (20)$$

The left inequality is the Szegő-Weinberger inequality and the right inequality is the Faber-Krahn inequality. The middle inequality is equivalent to $j'_{\frac{d}{2},1} \leq j_{\frac{d}{2}-1,1}$, which follows from $\mathcal{N}_{\mathbb{B}_d}^D(k) \leq \mathcal{N}_{\mathbb{B}_d}^N(k)$. For more details, see [7], [1] and [4].

By substituting (15) and (16) into (14). It can be seen that the Dirichlet eigenvalues of the disk are

$$\{\lambda_{nm}\} = \{j_{nm}^2 \mid \forall n \in \mathbb{N} \cup \{0\}, m \in \mathbb{N}\},$$

and the Neumann eigenvalues are

$$\{\mu_{nm}\} = \{(j'_{nm})^2 \mid \forall n \in \mathbb{N} \cup \{0\}, m \in \mathbb{N}\}.$$

As far as multiplicity, it should be noted that (15) and (16) are each describing two eigenfunctions for each set of indices, one for sine and one for cosine. However, when $n = 0$, $\sin(n\phi) = 0$, which isn't acceptable for eigenfunctions. Thus $j_{n,m}$ has multiplicity 1 when $n = 0$ and multiplicity 2 otherwise. Lastly, as can be seen in 2, $\frac{dJ_0}{dx}$ has a root at 0 which produces a non-zero constant Neumann eigenfunction that must be accounted for. With all this in mind, we can construct an algorithm for calculating the ECFs on the unit disk by using the local root finding `fsolve` algorithm to find the roots of Bessel functions below a given input k :

Algorithm 2 Calculating the Dirichlet ECF on a disk

Input Maximum value k

Step 1: init $nMax = \lfloor k \rfloor$

Step 2: **for** $n = 0, \dots, nMax$

- Find all roots of $J_n(x)$ on interval $[n, k]$
- If $n == 0$, assign root multiplicity 1, else assign multiplicity 2

Step 3: **Sort** eigenvalues in ascending order

Step 4: Iterate through the ordered list starting from the second element, and for each element add the multiplicity value of the previous element to that of the current element

Output Set of tuples of the eigenvalues and the number of eigenvalues less than or equal to that eigenvalue.

The Neumann ECF algorithm is similar but uses the derivatives of Bessel functions. The inequalities in (19) ensure that the interval $[n, k]$ collects all the roots of J_n smaller than k , and (18) ensures that $nMax$ is the highest order we need to check.

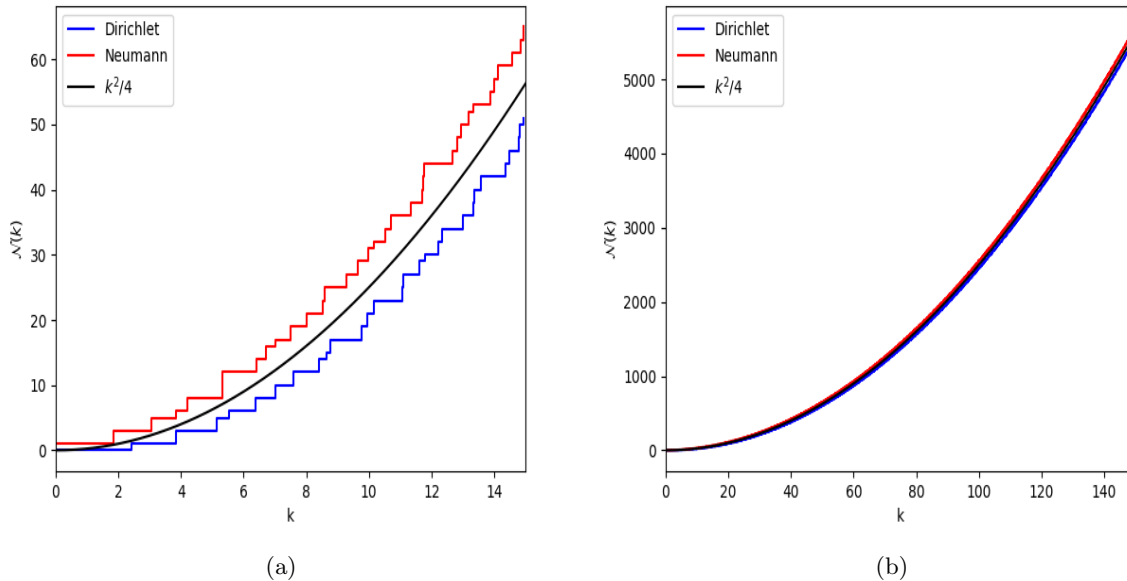


Figure 3: The Calculated ECFs and the leading Weyl Term on the Unit Disk up until (a) $k = 15$ and (b) $k = 150$

We implemented Algorithm 2 in Python using `fsolve` (see supplemental material) and Bessel function

implementations from the SciPy library, and the results are summarized in figure 3. As expected analytically, the Dirichlet and Neumann ECFs stay below and above the leading term respectively. The validity of our results is verified by comparison of figure 3a with figure 1 in [7], which is the same plot.

2.3 Comparison of 2D Geometries

We seek to compare a square and disk with equal area to visualize differences in lower-order asymptotics. The unit disk and square with sidelength $\sqrt{\pi}$ have the same area of π and thus the same leading Weyl term of $\frac{k^2}{4}$. Their difference lies in their perimeters, so they have different second Weyl asymptotics. The two-term Weyl asymptotics for the square with side length $\sqrt{\pi}$ and the unit disk are

$$\mathcal{N}_{\square}(k) = \frac{k^2}{4} \pm \frac{k}{\sqrt{\pi}} + o(k) \tag{21}$$

and

$$\mathcal{N}_{\circ}(k) = \frac{k^2}{4} \pm \frac{k}{2} + o(k) \tag{22}$$

respectively. Observe that as the unit disk has a smaller perimeter than the square with sidelength $\sqrt{\pi}$, its second Weyl term is smaller in magnitude than the square's second term. However, as can be seen in figure 4, this difference can be difficult to visualize with the standard ECF because the like $k^2/4$ term dominates the behavior of both functions for each shape. Thus, to highlight this difference, we also plotted one-term normalized ECFs defined by subtracting off the leading Weyl term for both the unit disk and the square. In general, we define the one-term normalized ECFs as

$$\mathcal{N}_{\Omega}^{(1)}(k) = \mathcal{N}_{\Omega}(k) - C_d|\Omega|_d k^d. \tag{23}$$

These new functions are visualized in figure 5 and illustrate the larger second Weyl term for the square.

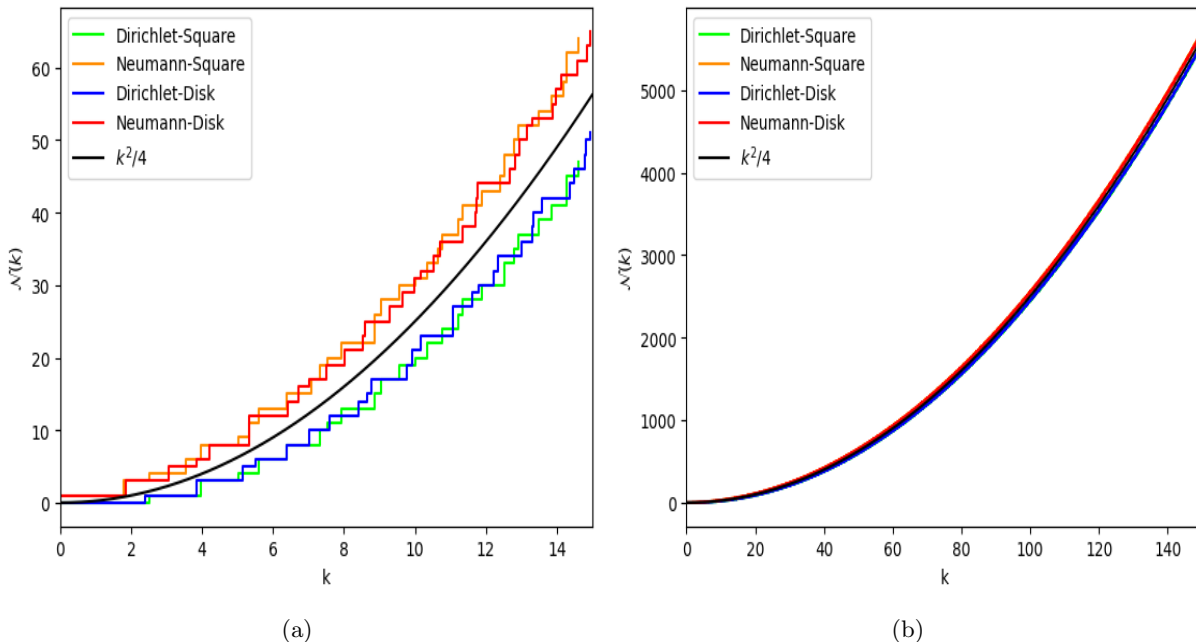


Figure 4: The Calculated ECFs and the leading Weyl Term for the Unit Disk and the Square with sidelength $\sqrt{\pi}$ up until (a) $k = 15$ and (b) $k = 150$

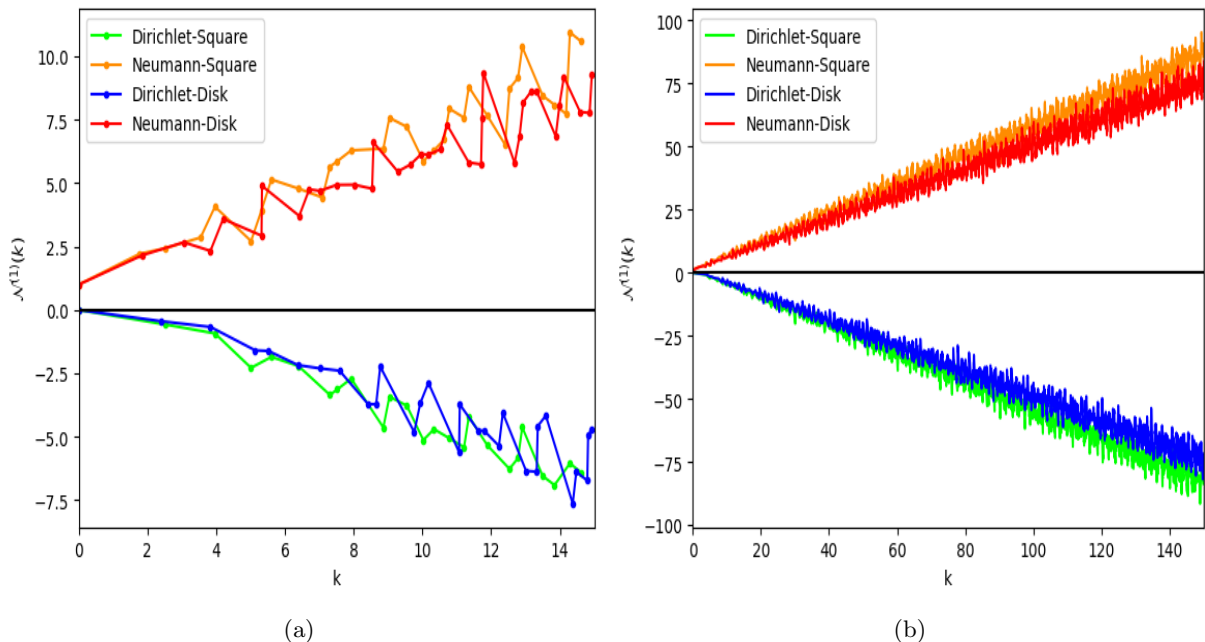


Figure 5: The one-term normalized ECFs for the Unit Disk and Square with sidelength $\sqrt{\pi}$ up to (a) $k = 15$ and (b) $k = 150$. Sampled points are where the original ECF changes.

3 3D Geometries

Now we move on to more complex geometries in \mathbb{R}^3 . We first examine the unit ball, then the unit cube, and finally the cylinder. Like all shapes in \mathbb{R}^2 , Weyl's law (5) regarding the leading asymptotic term is proven for these shapes. However, only the Dirichlet Polya Conjecture has been proven for the unit ball by Filonov et. al. in [7]. Therefore, we validate their Dirichlet proof and check the Neumann Polya Conjecture by calculating the ECFs of the Unit ball. Furthermore, since it is predicted by (6) that the leading terms $C_3|\Omega|_3k^3$ and $C_{b,3}|\partial\Omega|k^2$ are functions that solely depend on the volume and surface area of 3D shapes, we take as examples cylinders with the same volume and surface area of the unit cube. Per equation (6), the leading asymptotic term for the unit cube is

$$\mathcal{N}_\Omega(k) = \frac{k^3}{6\pi^2} + \frac{3k^2}{8\pi} + o(k^2). \quad (24)$$

As in the 2D section, by comparing the ECFs between a unit cube and some specific cylinders with identical predicted asymptotic terms, we can study what extra geometric features may be represented in these ECFs.

3.1 The Unit Ball

Our first 3D object is the ball with a unit radius and centered at the origin. Filonov et al. recently analytically proved the Dirichlet conjecture (i.e. Left inequality in (7)) for the unit ball [7]. We also know that the unit ball is a non-tiling subset of \mathbb{R}^3 . Thus, this half-proven conjecture marks the maiden attempt in a new area. In this section, we visualize this problem by calculating the ECFs on the ball. We use the following Spherical coordinate transformation $(x, y, z) \rightarrow (r, \phi, \theta)$, where r is the distance from the origin ϕ is the angle from the z -axis, and θ is the angle from the x -axis. The Helmholtz equation in Spherical polar coordinates is

$$\frac{\partial^2 u}{\partial r^2} + \frac{2}{r} \frac{\partial u}{\partial r} + \frac{1}{r^2} \frac{\partial^2 u}{\partial \phi^2} + \frac{\cos \phi}{r^2 \sin \phi} \frac{\partial u}{\partial \phi} + \frac{1}{r^2 \sin^2 \phi} \frac{\partial^2 u}{\partial \theta^2} = -\lambda u. \quad (25)$$

The Dirichlet BCs are $u(1, \phi, \theta) = 0$ and the Neumann BCs are $\frac{\partial u}{\partial r}|_{r=1} = 0$. It is also necessary to enforce periodicity on both θ and ϕ such that $u(r, \phi, \theta = 0) = u(r, \phi, \theta = 2\pi)$ and $u(r, \phi = 0, \theta) = u(r, \phi = \pi, \theta)$. With these BCs, separation of variables can be applied such that, for $n \in \mathbb{N} \cup \{0\}$ and $m \in \mathbb{N}$, the Dirichlet eigenfunctions on the unit ball are

$$u_{nm}(r, \phi, \theta) = \sqrt{\frac{\pi}{2s_{n,m}r}} \cdot J_{n+\frac{1}{2}}(s_{n,m}r) \sum_{t=-n}^n a_{nmt} \cdot \mathcal{Y}_n^t(\theta, \phi), \quad (26)$$

and the Neumann eigenfunctions are

$$u_{nm}(r, \phi, \theta) = \sqrt{\frac{\pi}{2s'_{n,m}r}} \cdot J_{n+\frac{1}{2}}(s'_{n,m}r) \sum_{t=-n}^n a_{nmt} \cdot \mathcal{Y}_n^t(\theta, \phi), \quad (27)$$

where a_{nmt} is a constant that depends on m , n , and t , $J_n(x)$ is the n th order Bessel function of the first kind, $s_{n,m}$ is the m th non-zero root of the n -order Spherical Bessel function of the first kind, $S_n(x)$, and $s'_{n,m}$ is the m th non-zero root of $\frac{dS_n}{dx}$. The functions of the angular parts ϕ and θ are combined into a spherical harmonic, $\mathcal{Y}_n^t(\theta, \phi)$, with $t = \{-n, \dots, 0, \dots, n\}$. For more details, see chapter 12 in [14].

It is now necessary to describe Spherical Bessel functions and their properties.

Definition 3.1.1 Spherical Bessel functions of order n are solutions to the following differential equation:

$$x^2 \frac{d^2 y}{dx^2} + 2x \frac{dy}{dx} + (x^2 - n(n+1))y = 0. \quad (28)$$

As a second-order differential equation, (28) also has two independent solutions, denoted S_n and Y_n . However, Y_n diverges at zero and therefore is not continuous on $[0, 1]$ and can't be used to construct valid solutions to (25). S_n takes the form $S_n(x) = \sqrt{\frac{\pi}{2x}} J_{n+\frac{1}{2}}(x)$, and thus defines the radial component of the eigenfunctions of the unit ball.

Remark: Equation (28) allows valid solution for any real number n , but the only valid solutions to (25) require the order n to be a non-negative integer.

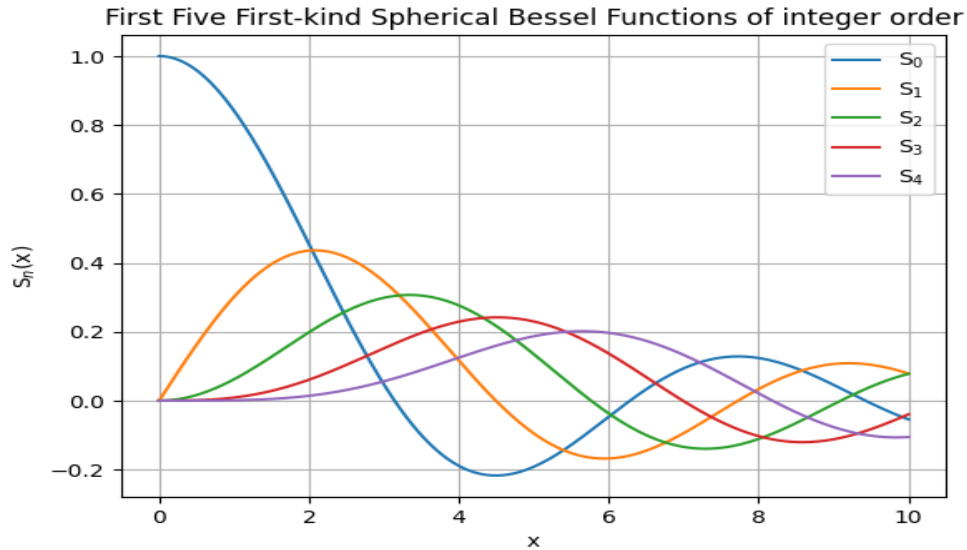


Figure 6: The First Five First-kind Spherical Bessel Functions of integer order, produced by Python Matplotlib

Figure 6 exhibits some relevant features of the Spherical Bessel functions. Just like the Bessel function in Figure 2, the Spherical Bessel functions are also oscillatory, and the roots also "cross" the x-axis regularly. Meanwhile, the distribution of their roots has similar characteristics. Every S_n with $n > 0$ has a trivial root at zero and they still satisfy inequalities (18) and (19). For more details, see [13]. By plugging both (26) and (27) into the Helmholtz equation (25), we can see that the Dirichlet and Neumann eigenvalues are

$$\{\lambda_{nm}\} = \{s_{n,m}^2 \mid \forall n \in \mathbb{N} \cup \{0\}, m \in \mathbb{N}\},$$

and

$$\{\mu_{nm}\} = \{(s'_{n,m})^2 \mid \forall n \in \mathbb{N} \cup \{0\}, m \in \mathbb{N}\},$$

respectively.

To calculate the multiplicity of each eigenvalue, observe that in the eigenfunction equations (26) and (27) there are $2n + 1$ independent spherical harmonics of order n . Therefore, the eigenvalues λ_{nm} and μ_{nm} both admit $2n + 1$ linearly independent eigenfunctions and have multiplicity $2n + 1$. Last but not least, as can be seen in figure 6, $\frac{dJ_0}{dx}$ also has a root at 0 which produces a non-zero constant Neumann eigenfunction that has to be covered in our counting functions. Here we construct a new algorithm for calculating the ECFs on the unit ball by using the structure in algorithm (2).

Algorithm 3 Calculating the Dirichlet ECF in a Ball

Input Maximum value k

step 1: init $nMax = \lfloor k \rfloor$

step 2: for $n = 0, \dots, nMax$

- Find all roots of $S_n(x)$ on interval $[n, k]$
- Assign root multiplicity $2n + 1$

step 3: Sort eigenvalues in ascending order

step 4: Iterate through the ordered list starting from the second element, and for each element add the multiplicity value of the previous element to that of the current element

Output Set of tuples of the eigenvalues and the number of eigenvalues less than or equal to that eigenvalue.

The Neumann ECF algorithm is similar but uses the derivatives of Spherical Bessel functions. Additionally, we manually add the first eigenvalue $\mu_{nm} = 0$ with multiplicity 1 in our Neumann algorithm. The inequalities in (19) ensure that the interval $[n, k]$ collects all the roots of S_n smaller than k , and (18) ensures that $nMax$ is the highest order we need to check.

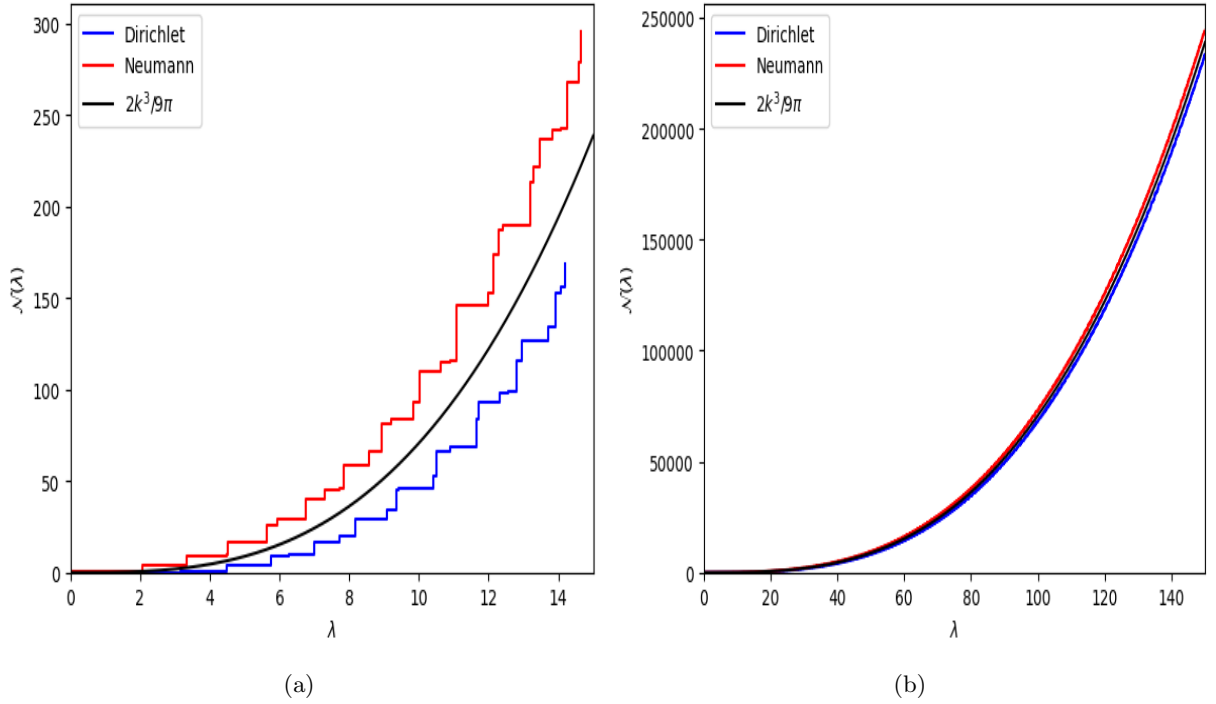


Figure 7: The Calculated ECFs and the leading Weyl Term on the unit ball up until (a) $k = 15$ and (b) $k = 150$

We implemented Algorithm (3) in Python using `fsolve` and Spherical Bessel function implementations from the SciPy library, results are shown in figure 7. As expected analytically, the Dirichlet ECF stays below the Weyl leading term. Furthermore, the calculated Neumann ECF stays above the Weyl leading term for the range checked up to $k=150$, giving positive evidence to the Neumann Polya Conjecture on the unit ball.

3.2 The Unit Cube

We now consider the ECFs of geometries where Polya's conjecture is proven, so that we might compare their counting functions. We start with the cube. We limit our focus to the unit cube, but the ECF results can be extended to arbitrary cubes similar to the arbitrary square considered in Section 2.1. We include the eigenvalues and eigenfunctions here for the sake of completeness. Just as in the 2D case, the Helmholtz equation in 3D Cartesian coordinates is

$$\frac{\partial^2 u}{\partial x^2} + \frac{\partial^2 u}{\partial y^2} + \frac{\partial^2 u}{\partial z^2} = -\lambda u. \quad (29)$$

With Dirichlet BCs and applying the method of separation of variables, we see that the Dirichlet eigenfunctions are

$$u_{nml}(x, y) = \sin(n\pi x) \cdot \sin(m\pi y) \cdot \sin(l\pi z), \quad (30)$$

and with Neumann BCs we see that the Neumann eigenfunctions are

$$u_{nml}(x, y) = \cos(n\pi x) \cdot \cos(m\pi y) \cdot \cos(l\pi z). \quad (31)$$

These can be applied to (29) to find that the eigenvalues are

$$\lambda_{nml} = \pi^2(n^2 + m^2 + l^2), \quad (32)$$

where $n, m, l \in \mathbb{N}$ in the Dirichlet case and $n, m, l \in \mathbb{N} \cup \{0\}$ in the Neumann case. The ECFs of the cube can be computed by simply modifying algorithm 1 to include a third for loop to account for the new index. ECFs results for the unit cube can be seen in figure 8 in section 3.4.

3.3 The Cylinder

The last 3D geometry we study is the Cylinder with radius R and height h , $C_{R,h}$. Observe that the Polya conjecture for the cylinder is true as a corollary to Filonov et. al.'s proof of the Unit Disk. This is because $C_{R,h} = D_R \times [0, h]$, with D_R the disk of radius R , satisfies the conditions of Proposition 1.4. Thus, our interest lies not in numerically checking Polya's conjecture but in comparing computed ECFs to find evidence of meaningful differences in eigenvalue distribution between different shapes. We use the cylindrical coordinate system defined by the map $(x, y, z) \rightarrow (r, \phi, z)$ where r is the distance from the z -axis and ϕ is the angle from the x -axis. The Helmholtz equation is expressed in this coordinate system as follows:

$$\frac{\partial^2 u}{\partial r^2} + \frac{1}{r} \frac{\partial u}{\partial r} + \frac{1}{r^2} \frac{\partial^2 u}{\partial \phi^2} + \frac{\partial^2 u}{\partial z^2} = -\lambda u. \quad (33)$$

The Dirichlet BCs in this coordinate system are $u(R, \phi, z) = u(r, \phi, 0) = u(r, \phi, h) = 0$ and the Neumann BCs are $\frac{\partial u}{\partial r}|_{r=R} = \frac{\partial u}{\partial z}|_{z=0} = \frac{\partial u}{\partial z}|_{z=h} = 0$. While separation of variables can once again be utilized to generate the eigenfunctions and determine the eigenvalues that way, due to the previously stated Cartesian product definition of the cylinder, it is possible to define the eigenvalues of the cylinder in terms of the eigenvalues of the disk and the interval:

Theorem 3.3.1 The eigenvalues of the cylinder $C_{R,h}$ in the Dirichlet case are defined as

$$\lambda_{nml}(R, h) = \frac{j_{nm}^2}{R^2} + \frac{k^2 \pi^2}{h^2}, \quad (34)$$

and the eigenvalues in the Neumann case are

$$\lambda_{nml}(R, h) = \frac{(j'_{nm})^2}{R^2} + \frac{k^2 \pi^2}{h^2}, \quad (35)$$

where $n \in \mathbb{N} \cup \{0\}$, $m \in \mathbb{N}$, in the Dirichlet case $l \in \mathbb{N}$ and in the Neumann case $l \in \mathbb{N} \cup \{0\}$.

Proof The Dirichlet proof can be found in [3], and the Neumann proof follows from the same method.

Similar to the square and cube, the multiplicity of a given eigenvalue is a nontrivial problem based on the parameters of a particular cylinder. [3] gives more detail about the multiplicity of Dirichlet eigenvalues. Again similar to the square and cube, we circumvent this problem by using a naive algorithm first to generate every eigenvalue on the disk and interval independently and then check every possible sum between these two sets to see if it is below our given bound.

Algorithm 4 Calculating the Dirichlet ECF on a Cylinder

Input Maximum value k

Step 1: init $lMax = \lfloor \frac{kh}{\pi} \rfloor$

Step 2: init eigenvalues as an empty list

Step 3: Using algorithm 2, make list λ of all disk eigenvalues below k^2

Step 4:

For $l = 1, \dots, lMax$

· **For** λ_{nm} in λ

· Find candidate $\lambda_{nml} = \lambda_{nm} + \frac{l^2\pi^2}{h^2}$

· **If** candidate $\lambda_{nml} > k^2$, break

· **Elseif** candidate not in eigenvalues, add to eigenvalues with multiplicity 1 if $n == 0$ or multiplicity 2 if $n > 0$

· candidate is in eigenvalues, multiplicity $+= 1$

Step 5: **Sort** eigenvalues in ascending order

Step 6: Iterate through the ordered list starting from the second element, and for each element add the multiplicity value of the previous element to that of the current element

Output Set of tuples of the eigenvalues and the number of eigenvalues less than or equal to that eigenvalue.

3.4 Comparison of 3D Geometries

To compare the unit cube and cylinders of equal volume and surface area, we must first construct such cylinders. Two variables define a unique cylinder, the radius r and height h . Given that we have two constraint equations on the volume and surface area, this is a fully defined problem that produces the following polynomial when solved:

$$\pi x^3 - 3x + 1. \quad (36)$$

Specifically, the cylinder with r equal to a positive root of (36) and $h = \frac{1}{\pi r^2}$ has the same volume and surface area as the unit cube. In fact, (36) has two positive roots, $r_1 \approx 0.40071301$ and $r_2 \approx 0.713154$. From now on, we denote these cylinders as C_1 and C_2 . Recall that since C_1 , C_2 , and the unit cube share volume and surface area, they have the same predicted two-term Weyl asymptotics as per (24):

$$\mathcal{N}_\Omega(k) = \frac{k^3}{6\pi^2} \pm \frac{3k^2}{8\pi} + o(k^2).$$

As such, we expect them to have very similar ECFs, with any distinctions being defined by the $o(k^2)$ term. We are interested in evaluating what additional geometrical information may be involved with the $o(k^2)$ term, so we computed the ECFs for the three geometries and plotted them against each other. As with the 2D analysis, we also normalized the ECFs for each shape to emphasize the behavior of the $o(k^2)$ term. However, since the shapes are selected to have equal volume and surface area, in this case, we chose a two-term normalization. For an arbitrary ECF on geometry Ω , we define the two-term normalized ECF as

$$\mathcal{N}_\Omega^{(2)}(k) = \mathcal{N}_\Omega(k) - C_d |\Omega|_d k^d \mp C_{b,d} |\partial\Omega|_{d-1} k^{d-1}, \quad (37)$$

with a minus for the Neumann case and a plus for the Dirichlet case. Due to the heavy overlap of (37) between the Dirichlet and Neumann cases, they are split into two separate figures for clarity. The results are in figures 8-10.

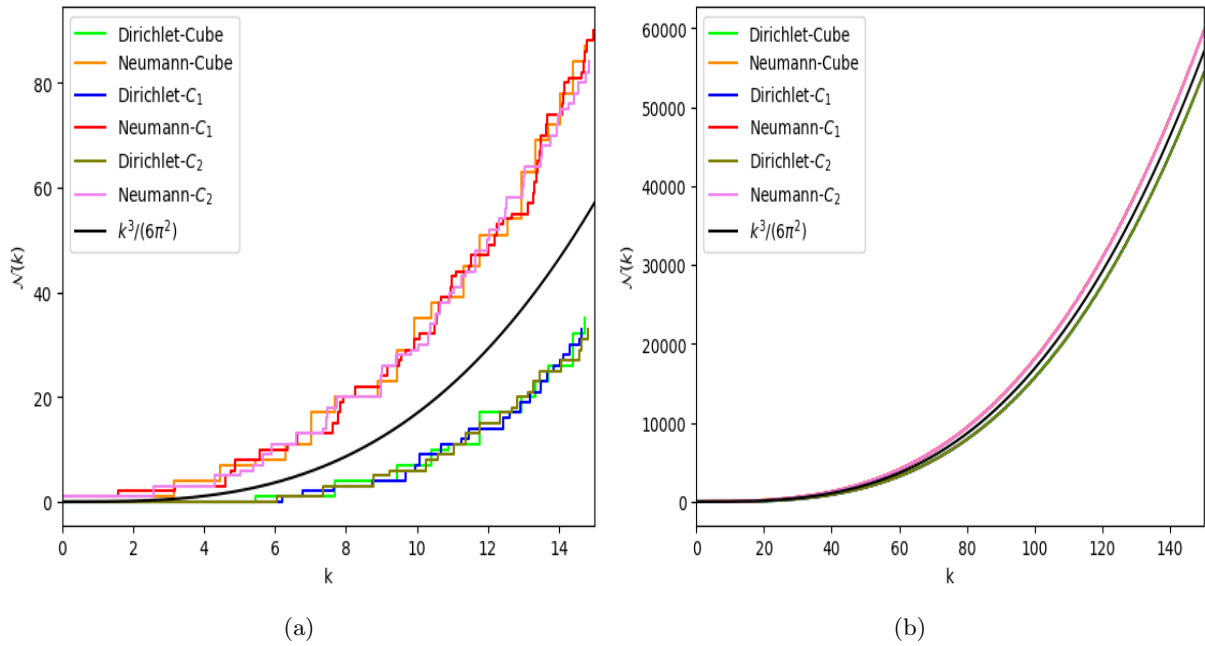


Figure 8: The Calculated ECFs and the leading Weyl Term for C_1 , C_2 and the Unit Cube up until (a) $k = 15$ and (b) $k = 150$

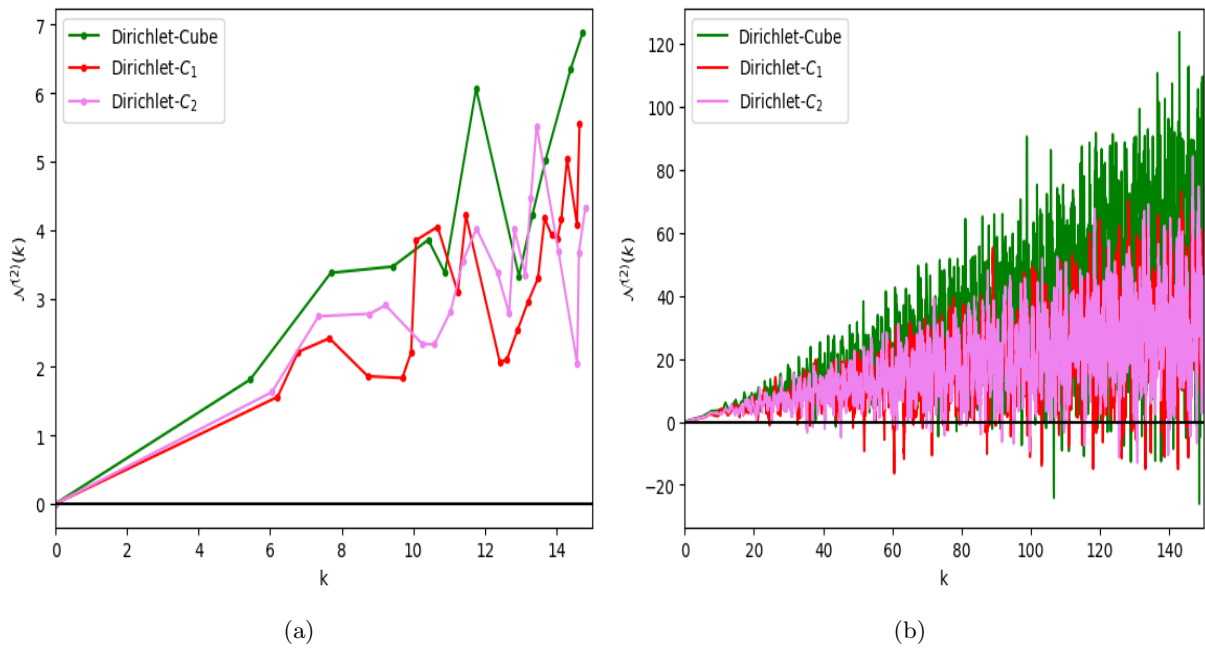


Figure 9: The two-term normalized Dirichlet ECFs for C_1 , C_2 , and the Unit Cube up to (a) $k = 15$ and (b) $k = 150$. Sampled points are where the original ECF changes.

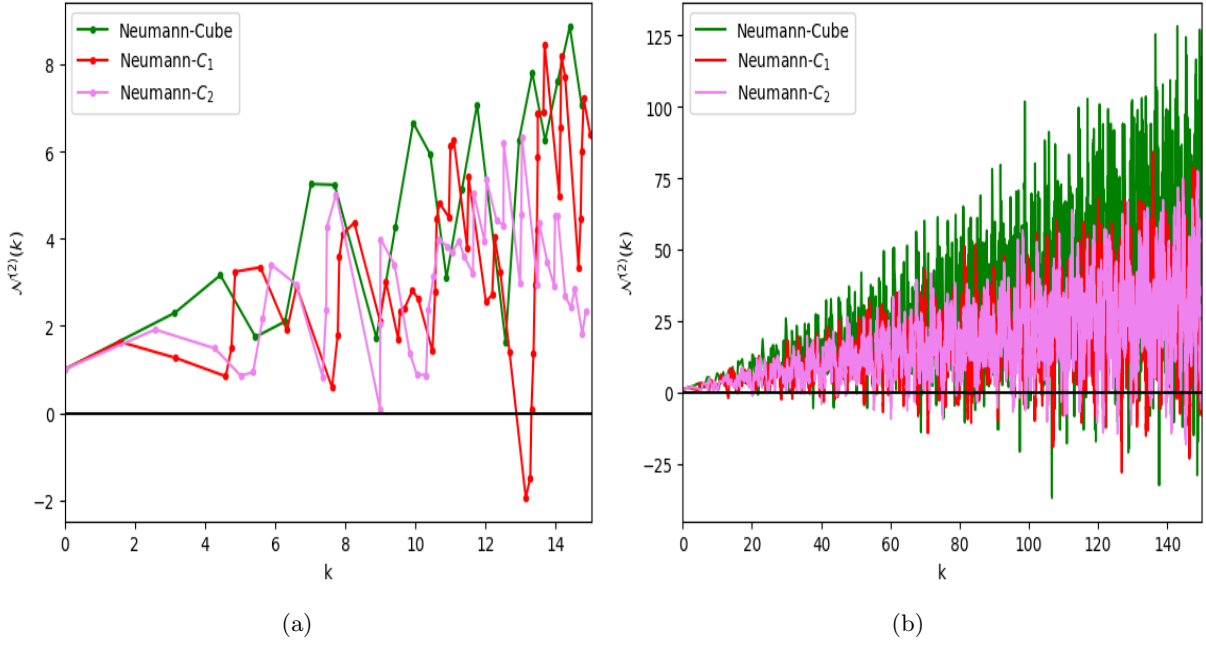


Figure 10: The two-term normalized Neumann ECFs for C_1 , C_2 , and the Unit Cube up to (a) $k = 15$ and (b) $k = 150$. Sampled points are where the original ECF changes.

As can be seen from figures 9b and 10b, there is certainly a difference in the behavior of the normalized ECFs for the different shapes. While the variance of these functions appears to grow as a function of k consistently, the variance for the two-term normalized ECF of the unit cube is greater than that of the cylinders, reaching higher maxima and lower minima. As the cylinders have very similar behavior, this could imply a functional difference between the ECFs for the cube and cylinder despite having the same volume and area. Furthermore, while they tend to stay positive most of the time, the normalized ECFs consistently fall below zero. Figure 10a shows the normalized ECF for C_1 going below zero very early, before $k = 14$. These crossings demonstrate that $\mathcal{N}_\Omega^N(k)$ is not always greater than $C_d|\Omega|_d k^d + C_{b,d}|\partial\Omega|_{d-1} k^{d-1}$ for $d = 3$.

4 Future Work

First of all, the set of 2D and 3D geometries we considered here is not exhaustive. In the 2D case, we could also consider the arbitrary parallelogram, which is interesting because it is still convex yet lacks the rotational symmetries of the disk or square. It would also be interesting to repeat the experiment of comparing shapes with the same area and perimeter for the 2D case, to see if there are distinctions like in the 3D case. While this experiment would be impossible using the unit disk, it could be done with other convex shapes like the aforementioned parallelogram or the ellipse. In 3D, further comparisons using objects with holes, such as a solid torus, could be intriguing. While it lacks an analytical Helmholtz solution, its eigenvalues can be computed with finite-element software like FEniCS [2].

Another way to study the $o(k^{d-1})$ term is to fit the normalized functions to polynomial or spline curves. Then, we could study the $o(k^{d-1})$ term by studying how the coefficients of fit change for different objects. It would also be interesting to construct a measure for the variance of the normalized functions for the 3D geometries as a function of k , and compare this measure for different shapes to see if there is any interesting information. Future research could also consider different normalizations for the ECFs.

One other type of normalization that could be considered is of the form $\frac{\mathcal{N}_\Omega^{(2)}(k)}{k^\alpha}$, $\alpha > 0$, which could force

the ECF to a constant value. This constant value could then be compared to geometric parameters of Ω to elucidate further information about the $o(k^{d-1})$ term.

Lastly, some improvements can be made to our numerical analysis. Currently, we use the default precision in Python, which is the same as the precision of Python float numbers. At the same time, when using `fsolve` to find roots, we chose error tolerance $xtol \leq 10^{-8}$ to balance the calculation speed and accuracy. It is known that Bessel functions "dampen" asymptotically, with an $(\frac{2}{\pi x})^{1/2}$ factor in the asymptotic expansion [16]. Therefore our fixed-precision root-finding method will fail to find sufficiently large roots. One method of resolving this could involve calling an external library such as `MPMath` [17] that provides data types with arbitrary precision. Another method could involve switching from root-finding algorithms and using matrix eigenvalue methods like those described in reference [9].

Acknowledgements

The authors would like to thank the Northeastern University Department of Mathematics, the Northeastern University College of Science, and the National Science Foundation for funding this project. Specifically, NSF funding came from the NSF-RTG grant "Algebraic Geometry and Representation Theory at Northeastern University" (DMS-1645877).

The authors also thank Zhaoming Li for her advice and support and the anonymous reviewers for their suggestions and feedback.

References

- [1] T. V. ANOOP, V. BOBKOV, AND P. DRÁBEK, *Szegő-weinberger type inequalities for symmetric domains with holes*, SIAM Journal on Mathematical Analysis, 54 (2022), p. 389–422, <http://dx.doi.org/10.1137/21M1407227>.
- [2] I. A. BARATTA, J. P. DEAN, J. S. DOKKEN, M. HABERA, J. S. HALE, C. N. RICHARDSON, M. E. ROGNES, M. W. SCROGGS, N. SIME, AND G. N. WELLS, *DOLFINx: The next generation FEniCS problem solving environment*, Dec. 2023, <https://doi.org/10.5281/zenodo.10447666>, <https://doi.org/10.5281/zenodo.10447666>.
- [3] V. BOBKOV, *May 15, 2018 - eigenvalues of cylinders*, 2018, <https://vladimir-bobkov.ru/blog/2018/05/Eigenvalues-of-cylinders.html> (accessed June 4, 2024).
- [4] L. BRASCO, G. DE PHILIPPIS, AND B. VELICHKOV, *Faber–krahm inequalities in sharp quantitative form*, Duke Mathematical Journal, 164 (2015), <https://doi.org/10.1215/00127094-3120167>, <http://dx.doi.org/10.1215/00127094-3120167>.
- [5] P. BUSER, J. CONWAY, P. DOYLE, AND K.-D. SEMMLER, *Some planar isospectral domains*, International Mathematics Research Notices, 1994 (1994), pp. 391–400, <https://doi.org/10.1155/S1073792894000437>.
- [6] L. C. EVANS, *Partial Differential Equations Second Edition*, American Mathematical Society, 2010.
- [7] N. FILONOV, M. LEVITIN, I. POLTEROVICH, AND D. A. SHER, *Pólya’s conjecture for euclidean balls*, *Inventiones mathematicae*, 234 (2023), p. 129–169, <https://doi.org/10.1007/s00222-023-01198-1>.
- [8] E. M. HARRELL AND J. STUBBE, *Two-term, asymptotically sharp estimates for eigenvalue means of the laplacian*, *Journal of Spectral Theory*, (2016), <https://api.semanticscholar.org/CorpusID:119325064>.

- [9] Y. IKEBE, Y. KIKUCHI, AND I. FUJISHIRO, *Computing zeros and orders of bessel functions*, Journal of Computational and Applied Mathematics, 38 (1991), pp. 169–184, [https://doi.org/https://doi.org/10.1016/0377-0427\(91\)90169-K](https://doi.org/https://doi.org/10.1016/0377-0427(91)90169-K).
- [10] R. KELLNER, *On a theorem of polya*, The American Mathematical Monthly, 73 (1966), pp. 856–858, <http://www.jstor.org/stable/2314181>.
- [11] J. R. KUTTLER AND V. G. SIGILLITO, *Eigenvalues of the laplacian in two dimensions**, SIAM Review, 26 (1984), pp. 163–193, 10.1137/1026033.
- [12] A. LAPTEV, *Dirichlet and neumann eigenvalue problems on domains in euclidean spaces*, Journal of Functional Analysis, 152 (1997), p. 531–545, <https://doi.org/10.1006/jfan.1997.3155>.
- [13] F. W. J. OLVER AND L. C. MAXIMON, *Chapter 10.21 bessel function zeros*, 2024, <https://dlmf.nist.gov/10.21>.
- [14] P. J. OLVER, *Introduction to Partial Differential Equations*, Undergraduate Texts in Mathematics, Springer, 2020.
- [15] Y. SAFAROV AND D. VASSILIEV, *The Asymptotic Distribution of Eigenvalues of Partial Differential Operators*, Translations of mathematical monographs, v. 155, American Mathematical Society, 1997.
- [16] N. SEKELJIC, *Asymptotic expansion of bessel functions; applications to electromagnetics*, Dynamics at the Horsetooth, 2A (2010).
- [17] THE MPMATH DEVELOPMENT TEAM, *mpmath: a Python library for arbitrary-precision floating-point arithmetic (version 1.3.0)*, 2023. <http://mpmath.org/>.
- [18] H. WEYL, *Ueber die asymptotische verteilung der eigenwerte*, Nachrichten von der Gesellschaft der Wissenschaften zu Göttingen, Mathematisch-Physikalische Klasse, 1911 (1911), pp. 110–117, <http://eudml.org/doc/58792>.
- [19] H. WEYL, *Das asymptotische verteilungsgesetz der eigenwerte linearer partieller differentialgleichungen (mit einer anwendung auf die theorie der hohlraumstrahlung)*, Mathematische Annalen, 71 (1912), pp. 441–479, <https://doi.org/10.1007/BF01456804>, <https://doi.org/10.1007/BF01456804>.

A List of Symbols

| Symbol | Definition |
|-------------------------------|--|
| Ω | Subset of \mathbb{R}^d |
| k | Input of our eigenvalue counting functions |
| λ | Eigenvalue |
| μ | Neumann eigenvalue |
| C_d | Weyl constant: $\frac{1}{(4\pi)^{\frac{d}{2}} \Gamma(\frac{d}{2}+1)}$ |
| $C_{b,d}$ | Lower Weyl Constant: $\frac{C_{d-1}}{4}$ |
| Spherical Coordinates | θ : Angle from the x -axis, ϕ : angle from the z -axis |
| $J_n(x)$ | n th order Bessel Function of 1st kind |
| j_{nm} | The m th non-zero root of $J_n(x)$ |
| j'_{nm} | The m th non-zero root of $\frac{dJ_n}{dx}$ |
| $S_n(x)$ | n th order Spherical Bessel Function of 1st kind |
| s_{nm} | The m th non-zero root of $S_n(x)$ |
| s'_{nm} | The m th non-zero root of $\frac{dS_n}{dx}$ |
| $\mathcal{N}_\Omega^{(1)}(k)$ | The one-term normalized ECF |
| $\mathcal{N}_\Omega^{(2)}(k)$ | The two-term normalized ECF |